Geophys. J. Int. (2006) **166,** 579–589 doi: 10.1111/j.1365-246X.2005.02778.x

The Eifel Plume—imaged with converted seismic waves

Martin Budweg,[1,*] Günter Bock† and Michael Weber[1,2]

[1] *GeoForschungsZentrum Potsdam, Telegrafenberg,* E325 D-14473-*Potsdam, Germany. E-mail: mhw@gfz-potsdam.de*
[2] *Universität Potsdam,* D-14471-*Potsdam, Germany*

Accepted 2005 August 8. Received 2005 August 4; in original form 2004 September 15

SUMMARY

Receiver functions (RF) are used to investigate the upper mantle structure beneath the Eifel, the youngest volcanic area of Central Europe. Data from 96 teleseismic events recorded by 242 seismological stations from permanent and a temporary network has been analysed. The temporary network operated from 1997 November to 1998 June and covered an area of approximately 400 × 250 km^2 centred on the Eifel volcanic fields.

The average Moho depth in the Eifel is approximately 30 km, thinning to *ca*. 28 km under the Eifel volcanic fields. RF images suggest the existence of a low velocity zone at about 60–90 km depth under the West Eifel. This observation is supported by *P*- and *S*-wave tomographic results and absorption (but the array aperture limits the resolution of the tomographic methods to the upper 400 km). There are also indications for a zone of elevated velocities at around 200 km depth, again in agreement with *S*-wave and absorption tomographic results. This anomaly is not visible in *P*-wave tomography and could be due to *S*-wave anisotropy. The RF anomalies at the Moho, at 60–90 km, and near 200 km depth have a lateral extent of about 100 km. The 410 km discontinuity under the Eifel is depressed by 15–25 km, which could be explained by a maximum temperature increase of +200°C to +300°C. In the 3-D RF image of the Eifel Plume we also notice two additional currently unexplained conversions between 410 and 550 km depth. They could represent remnants of previous subduction or anomalies due to delayed phase changes. The lateral extent of these conversions and the depression of the 410 km discontinuity is about 200 km. The 660 km discontinuity does not show any depth deviation from its expected value. Our observations are consistent with interpretation in terms of an upper mantle plume but they do not rule out connections to processes at larger depth.

Key words: crust, Eifel, plume, receiver function, seismology, upper mantle.

1 INTRODUCTION

An important topic of geoscientific research are mantle plumes, since they are an episodic and local phenomena which rise from the Earth's mantle and bring more energy and mass in single events to the Earth's surface than the other plate tectonic processes over long time spans.

Most plumes are located in oceans and are characterized at the surface by island (e.g. Iceland) or island chains/clusters (e.g. Hawaii, Cape Verde and Canary Island). Over the last few years oceanic plumes have been the focus of several tomographic and RF studies, see for example, the Society hotpot (Niu *et al.* 2002), Iceland (Shen *et al.* 1998, 2003) and Hawaii (Shen *et al.* 2003). Recent work by Li *et al.* (2000, 2003, 2004) on oceanic plumes, especially on the Hawaiian plume, shows that even narrow structures (on the order of 100 km diameter) can be imaged by seismic methods. The advantage of the search for and studies of plumes situated under larger land masses, like the Tanzanian Craton (Brazier *et al.* 2000), the Yellowstone hotspot (see e.g. Fee & Dueker 2004) and the Eifel Plume in Central Europe (this study), is that does not require the logistically more challenging amphibious experiments needed to image oceanic plumes. This allows denser networks with higher spatial resolution to be deployed.

Some of the open questions concerning the Eifel Plume are:

(1) What is the source of the geodynamic activity,
(2) Does hot material rise from the Earth's mantle and if yes, from which depth,
(3) Can unusual structures and features produced by such processes be detected?

2 GEODYNAMIC SETTING

The geodynamic setting of the Eifel has been discussed in detail previously, see for example, Ritter (2005) for a recent introduction. Therefore, we limit ourselves to the main characteristics. The Eifel

*Now at: Texas Instruments Deutschland GmbH, Berlin, Germany.
†Günter Bock died tragically in a plane crash on 2002 November 6.

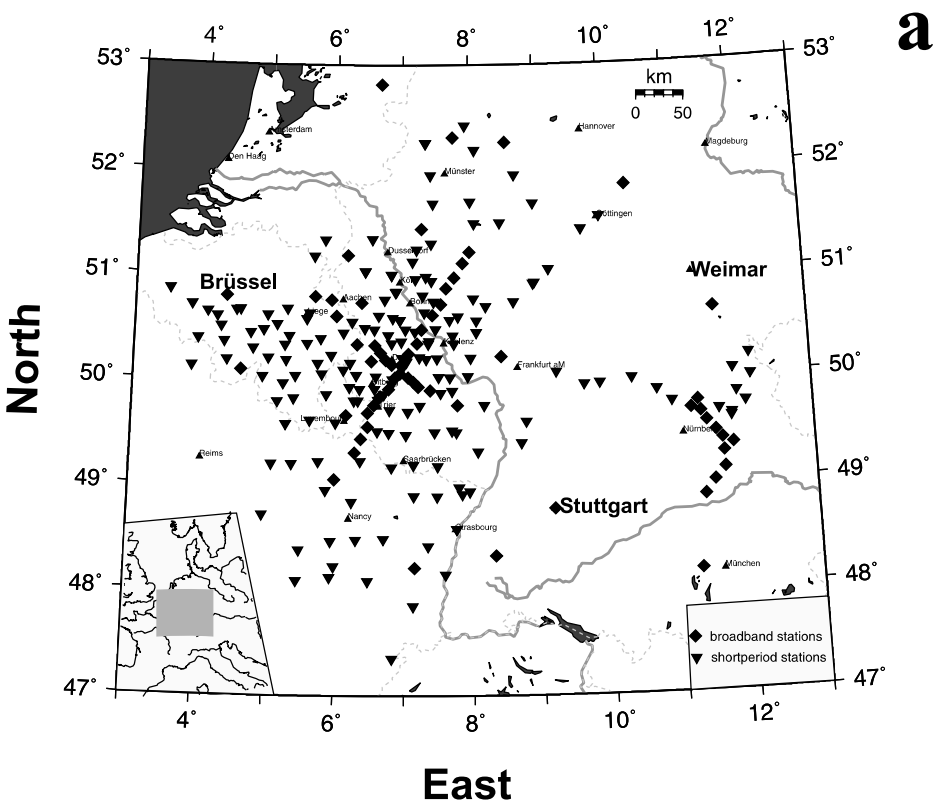

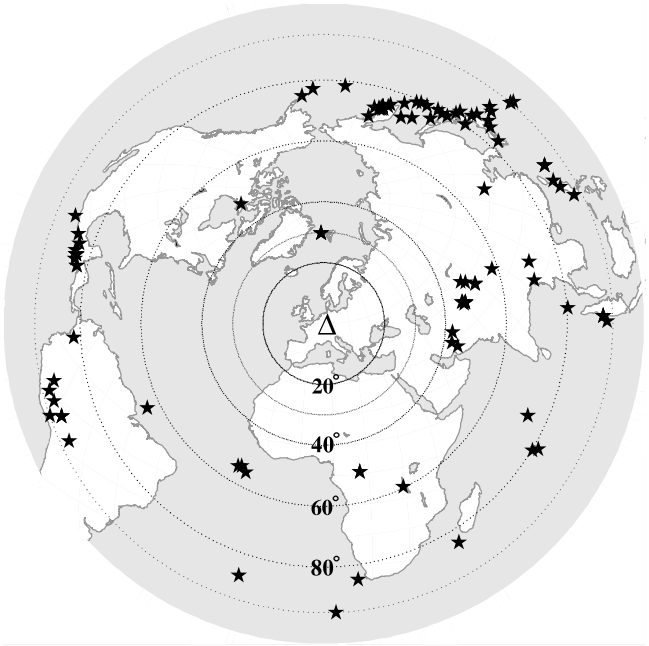

Figure 1. (a) Distribution of the 242 stations of the Eifel network (1997 November to 1998 June), including the permanent stations. The centre of the network is at the West Eifel. (b) Epicentral-equidistant map centred on the Eifel with the 96 teleseismic events used (mb >5.2, 30–95 degree).

region is part of the Rhenish Massif whose lithosphere consolidated during the Variscan orogeny. Following earlier volcanic episodes in the Cretaceous (∼108 Ma B.P.) and Tertiary (about 45 to 18 Ma B.P.), two volcanic fields evolved in the West and East Eifel starting about 700 to 600 ka B.P. (Lippolt 1983). The Quaternary volcanic activity resulted in about 350 eruptive centres (Schmincke *et al.* 1983) accompanied by strong uplift of locally more than 250 m (Meyer & Stets 1998). The most recent volcanic event was just 11 000 years ago (Brauer *et al.* 1999) and today a high flux of different magmatic gases and increased rates of mantle-derived gases are still

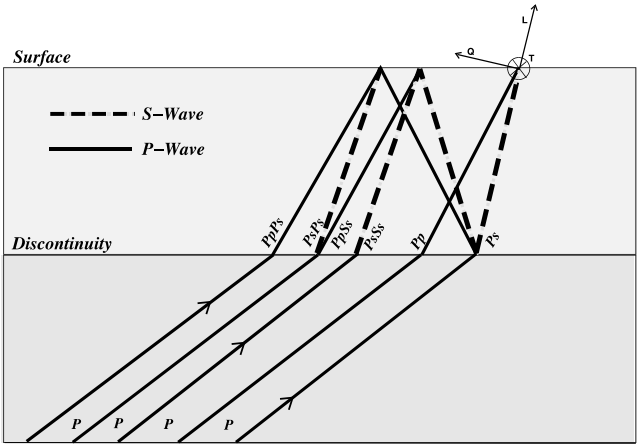

Figure 2. Sketch showing the ray path geometry used. The direct *P*wave, the converted *Ps* wave and multiples, for example, crustal multiples if the discontinuity is the Moho, are observed at the seismometer. Rotation to ray coordinates L, Q, T divides the energy into *P*, *SV* and *SH* energy, respectively.

observed (Griesshaber *et al.* 1992). The intraplate magmatism under the Eifel has previously been attributed to a major European hotspot (Duncan *et al.* 1972); however, the proposed age progression of volcanic centres is missing.

Wide-angle refraction seismic studies show a variation of the crustal thickness in the Rhenish Massif between 29 and 33 km (see e.g. Mechie *et al.* 1983). An initial tomographic experiment showed a low-velocity body with a diameter of about 200 km in the upper mantle down to about 200 km depth (Raikes & Bonjer 1983), interpreted as mantle diapir (Neugebauer *et al.* 1983). Similar low-velocity anomalies were found also in later studies with lower resolution (e.g. Spakman *et al.* 1993; Passier & Snieder 1996). The teleseismic *P*-wave tomography, using data of the Eifel Plume experiment (Ritter *et al.* 2000) shows a plume-like low-velocity structure, starting at about 70–80 km depth and extending downwards to more than 400 km depth (Ritter *et al.* 2001) centred on the southern part of the West Eifel volcanic field. The lateral dimension of the structure is about 100 km and the *P*-wave velocity contrast reaches −2.0 per cent. A similar structure with velocity reductions of up to −5 per cent is found by analysing traveltime residuals of teleseismic *S* waves (Keyser *et al.* 2000, 2002) in mostly the same locations. These results are furthermore corroborated by the detection of increased absorption and scattering in areas of low *S* velocities (Ritter & Meyer 2004; Rothert & Ritter 2000; Meyer *et al.* 2004; Hock *et al.* 2004). Additional and independent information about the structure of the mantle under the Eifel comes from a RF method study of data from the German Regional Seismic Network that detected a down-warping of the 410 km discontinuity underneath the Eifel region (Grunewald *et al.* 2001). On a more global scale Goes *et al.* (1999, 2000) mapped a mantle plume in the lower mantle underneath Central Europe, which may feed or have fed the Cenozoic volcanic fields in the region. However, the exact relationship and the dynamics of this deep-seated low-velocity structure to the shallower mantle Eifel Plume are not yet resolved.

3 DATA ACQUISITION AND PROCESSING

3.1 Sources and receivers

Within the Eifel Plume Project (www.uni-geophys.gwdg.de/∼eifel) a consortium of 10 European institutions operated a seismic network with an aperture of nearly 500 km by 500 km (Fig. 1a). 158 mobile recording stations were deployed between 84 permanent stations from 1997 November to 1998 June. Details on the design of the network and instrument types are given in Budweg *et al.* (1999) and Ritter *et al.* (2000). From the database with nearly 200 recorded teleseismic events we chose the 96 earthquakes with magnitude mb >5.2 in the distance range between 30 and 95 degrees (Fig. 1b). A list of the 96 events can be found in Budweg (2003).

3.2 Initial data processing

Since the data were recorded at different broad-band and short-period seismic stations the recorded traces were first resampled with 20 Hz and low-pass filtered with 8 Hz. Then the traces were restituted to true ground motion and bandpass filtered between 0.05 and 5 Hz.

The seismological method employed here, the receiver function (RF) method, uses three-component recordings to derive the Earth's structure. For overviews and some of the many applications of the method, with special emphasis on imaging plume structures, see for example, Vinnik (1977), Langston (1979), Ammon (1997), Shen *et al.* (1998, 2003), Li *et al.* (2000, 2003, 2004), Ryberg & Weber (2000), Grunewald *et al.* (2001), Niu *et al.* (2002) and Fee & Dueker (2004). The basic idea of the RF method is to use *P* to *S* converted seismic waves from zeroth-order discontinuities that arrive after the direct *P* wave, most strongly on the horizontal components (Fig. 2). Rotation in the ray coordinates L, Q, T and subsequent deconvolution of the Q with the L component gives the so called conversion operator for each source–receiver combination. These time traces are then migrated into the 3-D subsurface under the Eifel network; following an approach initially suggested by Yuan *et al.* (1997).

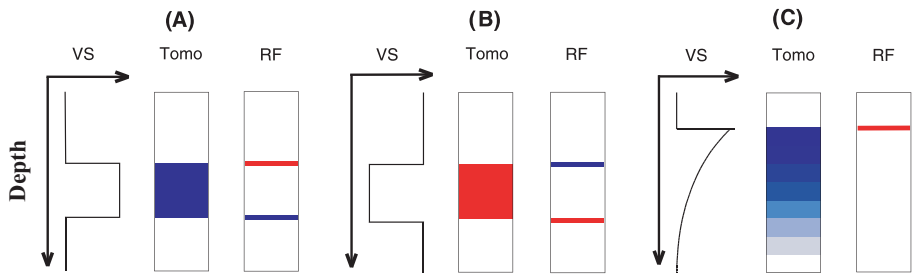

Figure 3. Images produced by teleseismic tomography (Tomo) and Receiver Functions (RF) for three types of velocity anomalies. (a) High-velocity zone. (b) Low-velocity zone. (c) Positive velocity jump with gradual decrease of velocity below. The same colour code is used throughout the paper.

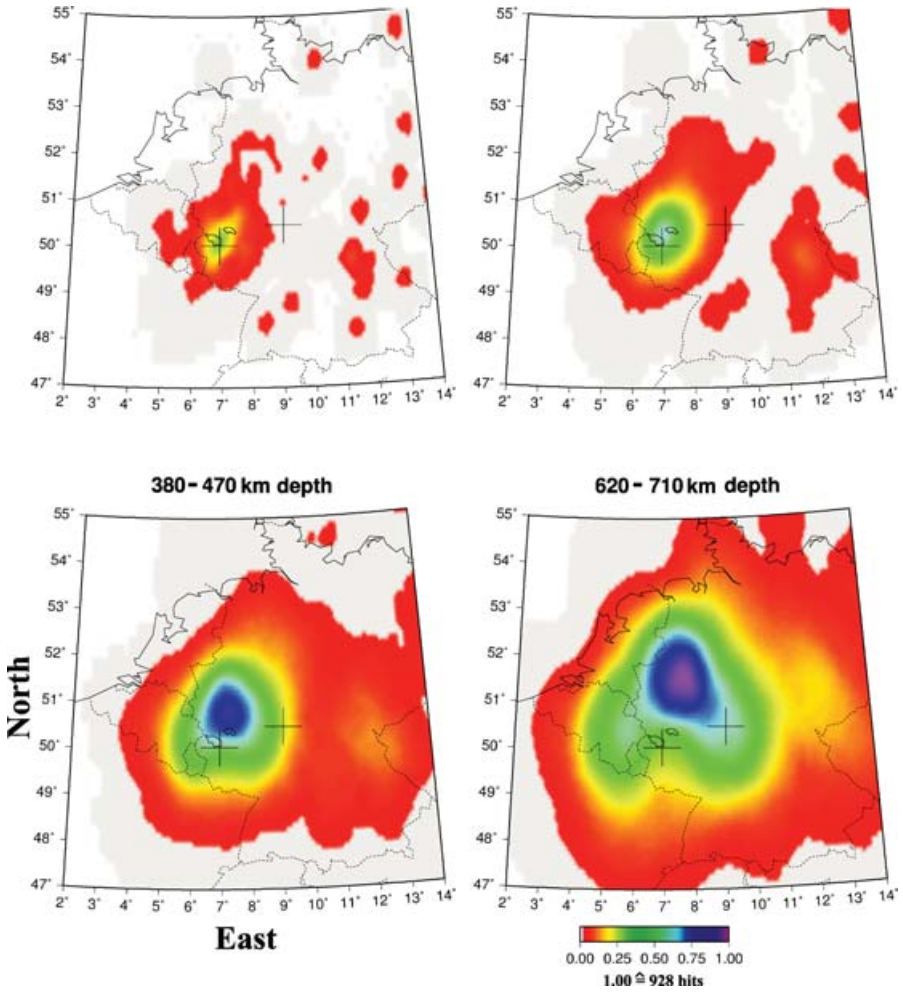

Figure 4. Horizontal slices at four depth ranges with their normalized average of hits per 5 × 5 × 2 km^3 volume element (voxel). A value of 1 indicates the maximum of 928 hits. Areas with an average of less than 20 hits are given in grey. The centre of the temporary network and the Tertiary volcano Vogelsberg are indicated by crosses. The eastern and western volcanic fields of the Eifel and political boundaries (dashed lines) are also indicated for orientation.

3.3 Comparison of tomographic and RF imaging results

To illustrate the resulting images and compare them to tomographic images Fig. 3 shows 1-D depth sections for a high-velocity *S*-velocity lid, a low-velocity zone and a high-velocity zone tapering off with depth, respectively. Whereas the high-velocity lid (Fig. 3a) is imaged in tomography, at least under ideal conditions, as a solid blue depth range, the RF method shows the zeroth-order jump at the top of the lid (with increasing depth: slow to fast = red) and the bottom (fast to slow = blue) of the lid. A reversed, but otherwise similar image is obtained for the low-velocity zone in Fig. 3(b). For a high-velocity lid with a gradual decrease of the velocity anomaly with depth, tomography images the tapering off of the velocity, whereas the RF method can only detect the zeroth-order contrast at the top of the lid (Fig. 3c), but not the gradual change below it unless the material properties change significantly over a short depth interval. For the typical 5 s dominant period of the converted waves used here that depth interval has to be less than 5–10 km, see also Bostock (1999). This shows that the two seismic methods, tomography and RF, nicely complement each other.

3.4 Processing and resolution

The depth migration follows closely the technique developed by Grunewald *et al.* (2001; Fig. 7), where individual RF time-series were mapped along their corresponding ray paths into the 3-D space. Here the subsurface is divided in 5 × 5 × 2 km^3 volume elements ('voxels') in which the different contributions from the migrated traces are then binned. To indicate the areas where the station and receiver combinations used (Fig. 1) gives a good coverage and resolution Fig. 4 shows the average of the hits in four depth intervals. With increasing depth more rays intersect and therefore the area of good coverage (blue and green colours with a maximum of 928 hits) increases. Areas with less than 20 hits per voxel are shown grey and will be blanked out in future slices through the 3-D subsurface under the Eifel area. The area of good resolution migrates north with increasing depth since most events are in the NE (see Fig. 1b).

4 RF MIGRATION RESULTS

4.1 Vertical slices through the 3-D migration volume

Fig. 5 shows a north–south and an east-west slice through the migrated 3-D volume (sum over the 45 voxels in a 2-degree-wide strip). The colour convention of Fig. 3 was used. To enhance the dominant features, a sliding window of 30 km width with 2 km step size was also used. Areas with reduced coverage are less bright. Here only a

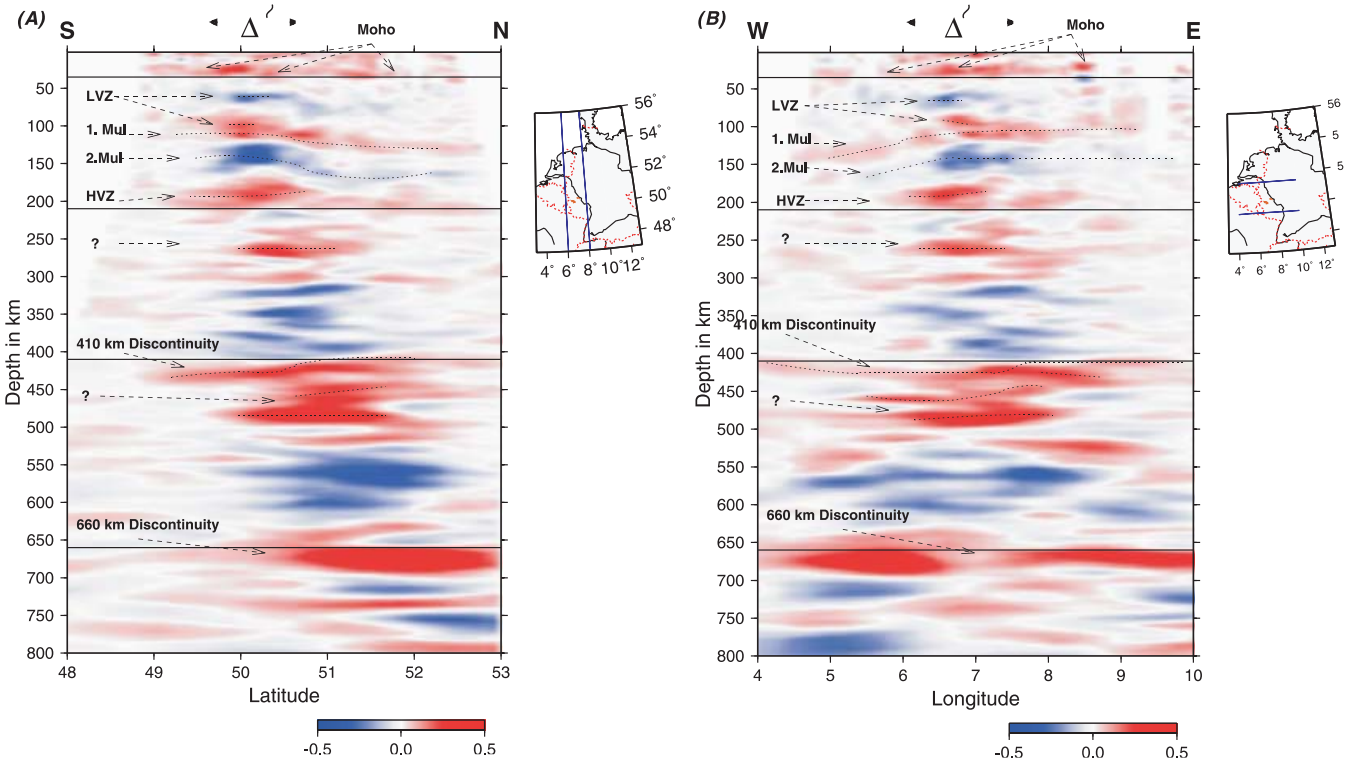

Figure 5. Sum over a 2-degree-wide strip (N–S (A) and E–W (B)) of depth migrated RF, for location see small inserts. Bright colours indicate better coverage (see also Fig. 4). The labels HVZ (LVZ) indicate a high-velocity zone (low-velocity zone) respectively. The dashed lines give the centre of each anomaly. The thin black horizontal lines correspond to the depth of 35 km (Moho depth according to the IASP91-model), the 210, the 410 and the 660 km discontinuity. The triangle at the top indicates the location of the Eifel volcanic fields and the black triangles outline the area of the Eifel.

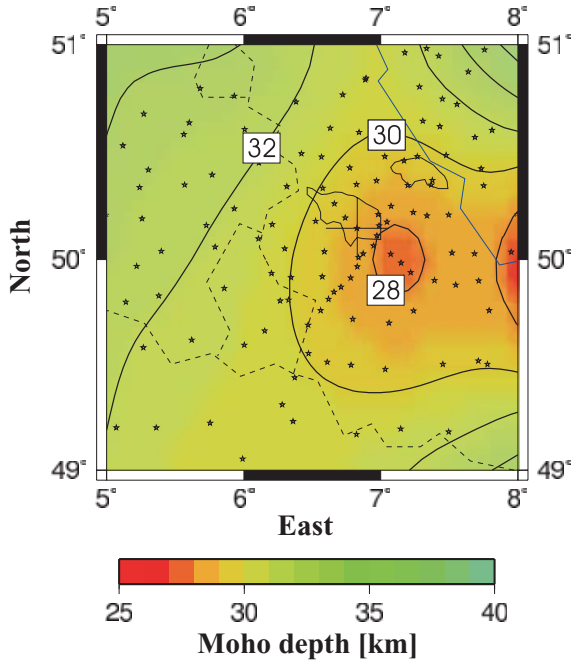

Figure 6. Moho depth as colour code and contour lines under the Eifel volcanic fields (solid lines) determined from migrated RF. The stars indicate the seismic stations and the dashed lines are the political borders.

first interpretation of the major features will be given, to be followed by a more detailed interpretation and discussion using forward modelling results and the comparison with tomography results in the next chapter.

At about 30 km depth in Fig. 5 the red feature (positive velocity jump with increasing depth) can be associated with the Moho that is elevated with respect to the ISAP91-model value of 35 km (Kennett & Engdahl 1991) indicated by the thin black line. The spatially co-located succession of blue and red at *ca*. 60 and 90 depth is interpreted as a low-velocity zone, see also Fig. 3(b). The red and blue features labelled 1. Mul and 2. Mul below 100 km depth with a joint move-out to larger depth towards the West are the expected crustal multiples (*P* and *S* multiples shown in Fig. 2). This identification is corroborated by the fact that they mimic the expected exaggerated topography of the crust. At *ca*. 200 km depth the red anomaly in Fig. 5 can be associated with the top of a high-velocity anomaly. The 410 km discontinuity is deflected 15–25 km downward followed at larger depth by two red anomalies indicative of positive velocity jumps, labelled with a question mark. The 660 km discontinuity is basically at the expected depth. In the following several of these features are discussed in more detail.

4.2 Moho

Fig. 6 shows a Moho depth map derived from the 3-D volume of the migrated data, see also Fig. 5 for two vertical sections through this volume. The map is centred on the Eifel, the area with the best resolution (Fig. 4, top left). A thinning of the Moho south of the two volcanic fields of the Eifel to about 28 km depth can be seen. This observation is in general agreement with previous wide-angle refraction seismic studies, that show a variation of the crustal thickness in the Rhenish Massif between 29 and 33 km (see e.g. Mechie *et al.* 1983). Due to the limited resolution of the RF method we cannot exclude, that these variations could also be due to the

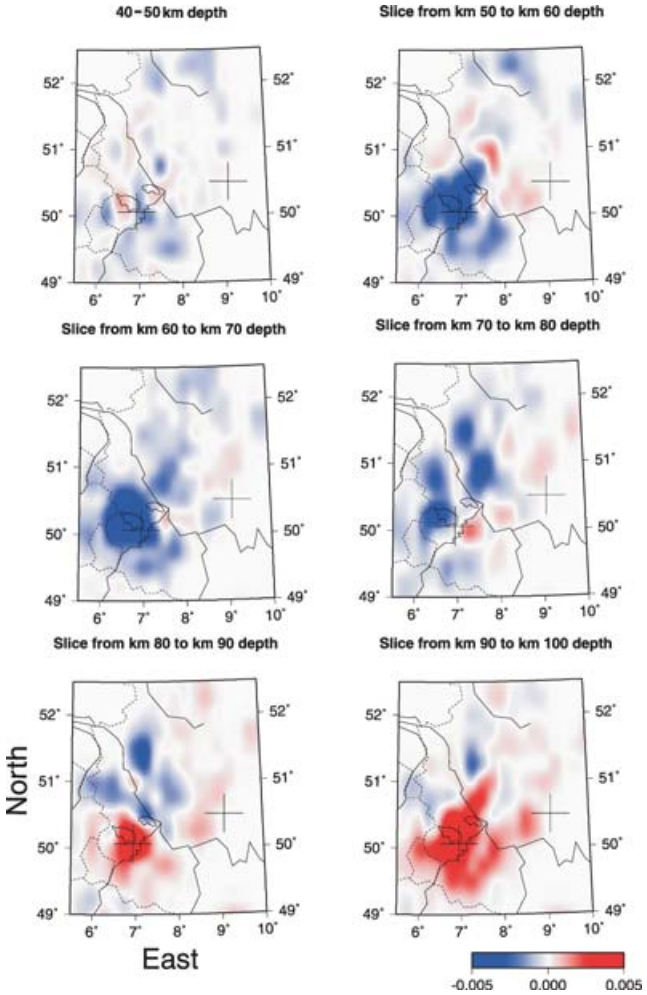

Figure 7. Horizontal slices averaged over 10 km thickness from the volume of the migrated RF for six depth ranges between 40 and 100 km depth. The volcanic fields of the Eifel are also outlined. The left cross is the centre of the Eifel network. The right cross shows the location of the Tertiary volcano Vogelsberg. A low velocity zone (LVZ) is observed between *ca*. 60 km depth (dark blue colours) and *ca*. 90 km depth (red colour; see also Fig. 3b). The bright red spots in the depth range between 90 and 100 km indicates the onset of first Moho multiples.

variation in crustal structure reported, for example, by the DEKORP Research Group (1991). The most straightforward interpretation for this crustal thinning is to link it to lateral displacement and stretching due to a plume. Note that the area east of 8°E is not well resolved at this depth (see Fig. 4, top left).

4.3 Low-velocity zone from 60 to 90 km depth

To ensure that the sequence in Fig. 7 of blue (at *ca*. 60 km depth) and red (at *ca*. 90 km depth) are indeed the top and bottom of a low-velocity zone (see also Fig. 3b) and not crustal multiples, inversions at several stations for velocity structure down 150 km were computed for stations showing a negative arrival 7 s after the first onset and also for stations not showing this arrival (for details see Budweg 2003). These inversions indicate that a low-velocity zone is required to explain this sequence of blue to red given in Fig. 7. This low-velocity zone is most strongly observed under the West Eifel and agrees well with the area with the strongest uplift (more than 250 m, Meyer & Stets 1998).

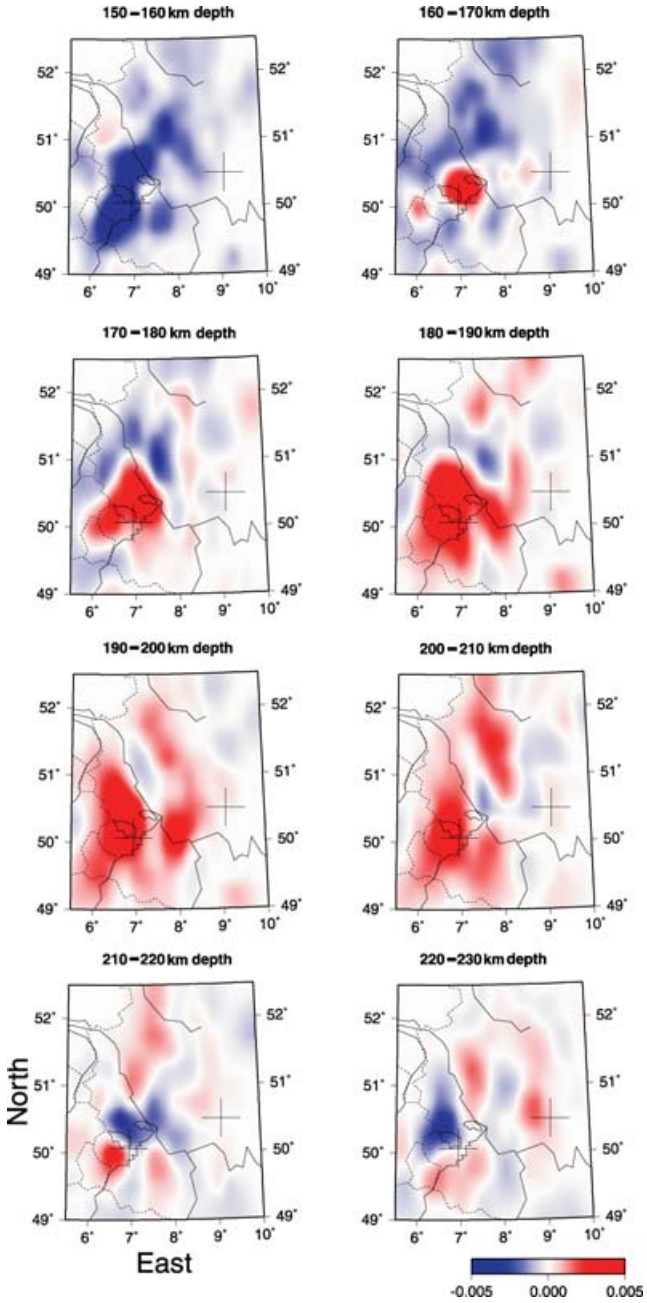

Figure 8. Horizontal slices averaged over 10 km thickness from the volume of the migrated RF for eight depth ranges between 150 and 230 km depth. The volcanic fields of the Eifel are also outlined. The left cross is the centre of the Eifel network. The right cross shows the location of the Tertiary volcano Vogelsberg. The bright red colours from 160 to 210 km depth indicate a conversion at a high-velocity contrast (see Fig. 3c).

Beginning at a depth of about 100 km (Fig. 7, bottom right and even better visible in Fig. 5) strong crustal multiples (red) appear over a large area. The identification of these arrivals as first crustal multiple (red, 1. Mul in Fig. 5) and the second crustal multiple at *ca*. 150 km depth (blue, 2. Mul in Fig. 5) was confirmed by forward modelling discussed in the next chapter.

4.4 High-velocity contrast at about 200 km depth

At about 200 km depth a strong (red) signal is visible in Fig. 8 and Fig. 5. The large amplitude of this arrival rules out, that this is the

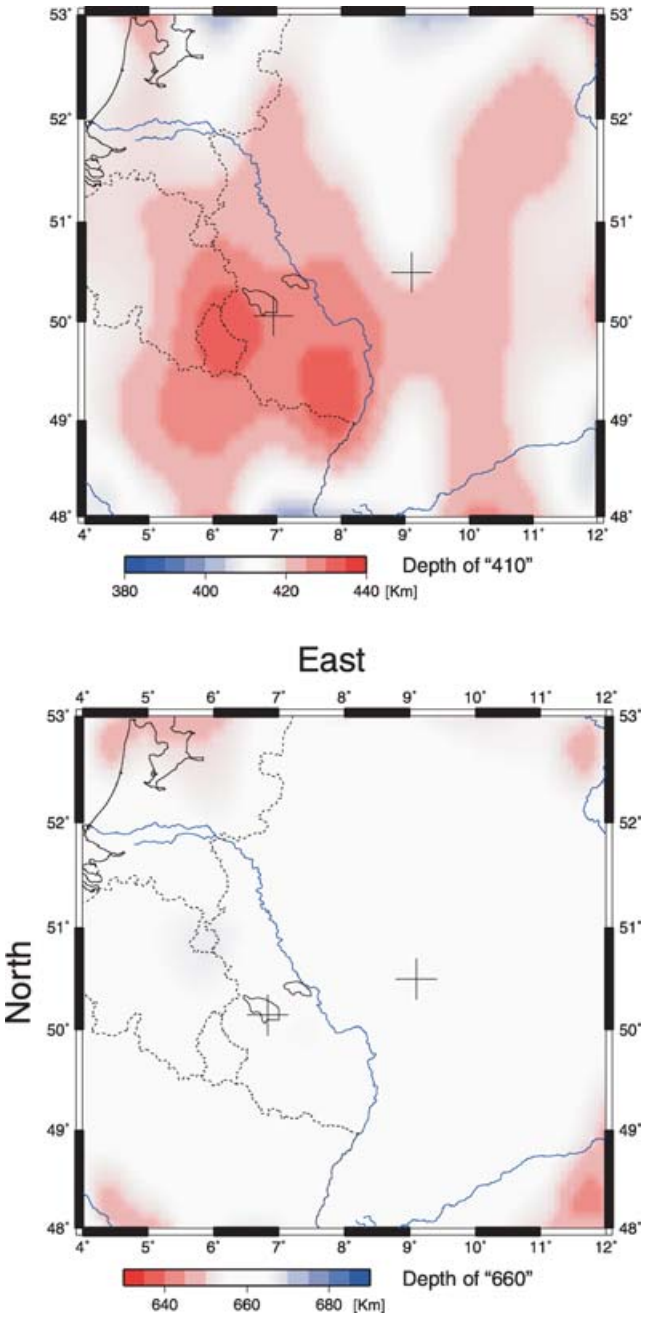

Figure 9. (Top) Topography of the 410 km discontinuity. South of the volcanic fields of the Eifel (solid lines and left cross) the 410 km discontinuity is depressed by about 15–25 km. (Bottom) Topography of the 660 km discontinuity. No deviation from the expected value of 660 km is observed.

third crustal multiple, for details see next chapter. Our preferred interpretation of this feature is a velocity structure similar to the one shown in Fig. 3(c), that is, a positive velocity contrast, tapering off with depth. Such an interpretation is supported by Keyser *et al.* (2002) in the *S*-wave tomography and will be discussed together with the *P*-wave tomography results of Ritter *et al.* (2000, 2001) in the last chapter.

4.5 The 410 km discontinuity

Due to the endothermic character of the 410 km phase transition a temperature increase will depress this phase boundary. Such a lowering of the 410 km discontinuity is visible in Fig. 5. To be able to gain an estimate of the lateral extent of the depression Fig. 9 (top) shows a map view of the effective conversion depth obtained in the depth range from 400 to 450 km averaged horizontally over 50 × 50 km cells, similar to Grunewald *et al.* (2001). The 410 km discontinuity is depressed under and south of the Eifel by 15 to 25 km. A similar depression in this region, but with much reduced lateral resolution due to the larger station spacing of the network used, was reported in Grunewald *et al.* (2001). With the Eifel Plume project data the lateral extent of the 15 km depression of the 410 km discontinuity can now be determined to be about 250 km. Within this area two regions of about 100 km diameter, one under Luxemburg and one southeast of it, seem to be depressed by up to 25 km.

The depth values given are almost independent from the velocity anomalies above the 410 km discontinuity, since *P* and *S* waves are both delayed by the low *P* and *S* velocities characterizing the Eifel plume (Ritter *et al.* 2001) and Keyser *et al.* (2000, 2002), respectively); see also Fig. 11. The small resulting difference between the delayed *P* and the delayed *S* wave gives a potential bias in the conversion depth of less than 2 km. The same argument also holds for the 660 km discontinuity.

4.6 The 660 km discontinuity

The effective conversion depth of the 660 km discontinuity, averaged horizontally over 50 × 50 km cells, is given in map view in Fig. 9 (bottom). Over the whole area, which is well resolved, see Fig. 4 (bottom right), the 660 km discontinuity seems to be unperturbed.

5 FORWARD MODELLING AND COMPARISON OF RF WITH TOMOGRAPHY RESULTS

To test the interpretations given in the last chapter, especially on thickness of the crust, the crustal multiples, the low-velocity body at about 60–90 km and the high-velocity body at about 200 km depth, we computed synthetic seismograms and processed them similar to the data (see chapter 3). For the forward modelling the algorithm of Ryberg *et al.* (2000, 2001, 2002), based on the Finite Difference Method of Kelly *et al.* (1976), was used. Unless otherwise noted, a constant vp/vs ratio of $(3)^{1/2}$ and Birch's law (Birch 1961) was assumed in the models. Small deviations from this value (Ritter *et al.* 2000; Keyser *et al.* 2000, 2002) do not change the results significantly.

All models used are 2-D with a box size of 5 degrees horizontally and 250 km deep, corresponding to the north–south transect in Fig. 5(a) centred on the Eifel. Receivers were placed at 5 km distances. The wavefields from 16 sources with offsets of 35–95 degrees from the north, and similar from the south, were computed assuming elastic media. Starting from a 2-D model with a thinned crust under the Eifel (from 30 to 28 km depth), crustal inhomogeneities (low-velocity sediments in the north), a low-velocity body (LVZ) and a high-velocity body (HVZ) in the upper mantle were added sequentially (Fig. 10, top left). This sequential modelling and processing allows isolating the effects and interaction of the different 2-D objects with the wavefield in the model, for details see Budweg (2003). The migrated RF result of the final model is given in Fig. 10 (right).

Fig. 10 (bottom left) shows a 2-D north–south slice of move-out corrected synthetic RF, that is, a section before depth migration. Starting from top, the strong crustal multiples (red and blue) in the

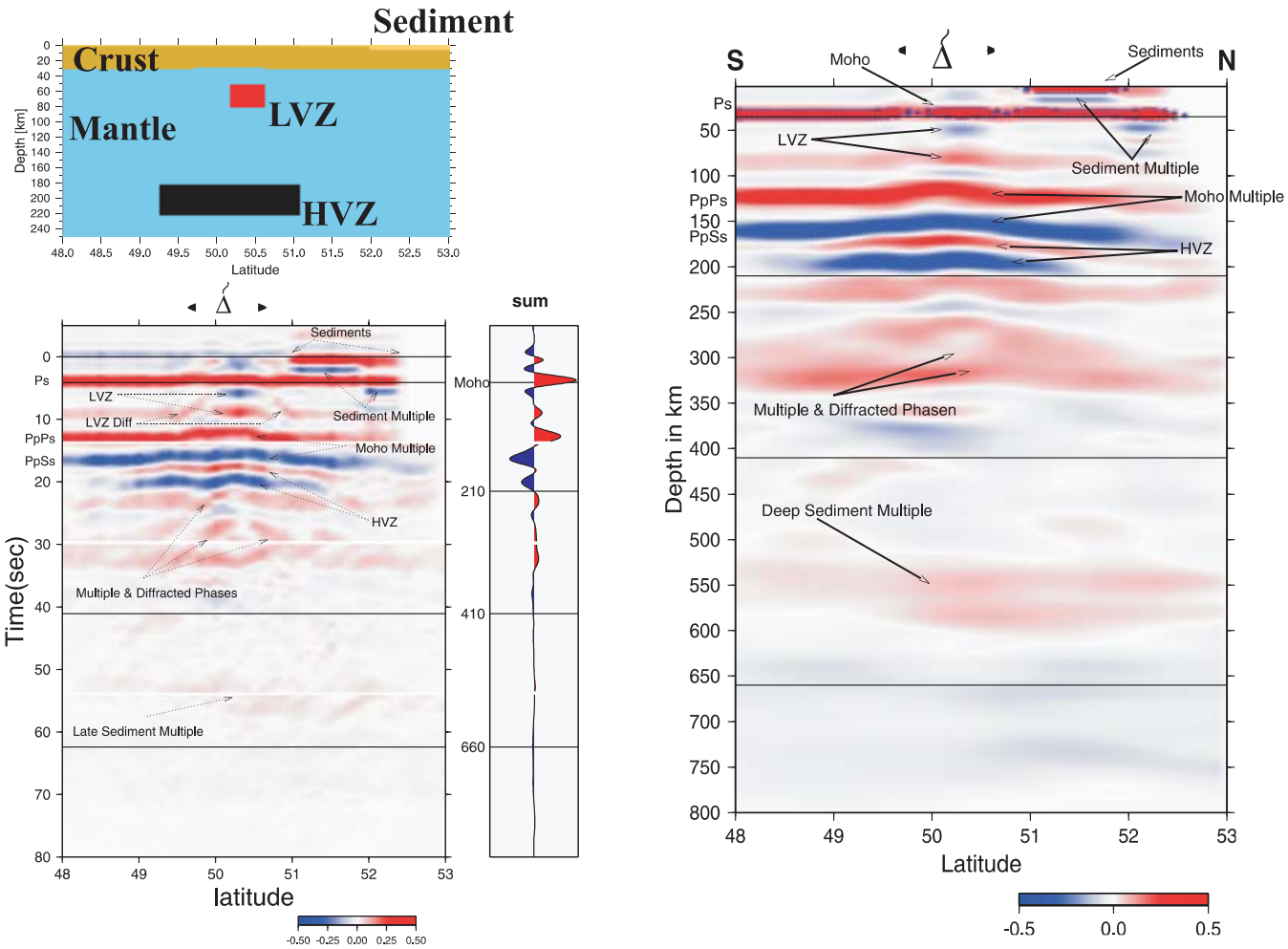

Figure 10. Results of the synthetic 2-D forward modelling. (Top left) 2-D model used. The *P* and *S* velocities of the sediments (upper right corner of model), the crust and the mantle are 4.0/2.22 km s^{-1}, 6.0/3.64 km s^{-1} and 8.2/4.73 km s^{-1}, respectively. Those for the low- and the high-velocity bodies are 7.7/4.45 km s^{-1} and 8.4/5.2 km s^{-1}, respectively. (Bottom left) Move-out corrected stacked time traces with phase labels on the left axis (for identification see Fig. 2). The time traces are sorted in each depth slice for the respective piercing points at 30, 210, 410 and 660 km depth and summed in 50-km-wide bins with 2 km distance increments. The triangle at the top indicates the location of the Eifel volcanic fields and the black triangles outline the area of the Eifel (see also Fig. 5). To the right the horizontal sum over all bins is shown. (Right) 2-D depth section from the migrated synthetics. All major features of the model can be identified. Higher multiples can be observed as weak and smeared out red regions down to the depth of the transition zone between 410 and 660 km.

low-velocity sediments in the north show up in the first 3 s, followed by the Moho conversion at 3.7 s and the PpPs and PpSs multiples at 12.7 s and 16.8 s, respectively (see also Ryberg & Weber 2000). The effect of the up-doming of the Moho is especially strong in the PpPs and PpSs multiples, because these phases sample the thinned crust three times (see Fig. 2). Later crustal multiples (five legs in the crust) are already significantly weaker, and would be even weaker, if realistic absorption, especially the strong absorption under the Eifel (Ritter 2006; Rothert & Ritter 2000), would have been included in the forward modelling.

The 20-km-thick and 50-km-wide LVZ produces the expected sequence of blue and red (see also Fig. 3b), with strong diffractions from the sharp corners of the LVZ (LVZ diffraction in Fig. 10, bottom left). Such a low-velocity body was observed as a −2 to −3 per cent velocity reduction in the *P*-wave tomography (Ritter *et al.* 2001) and a −2 to −5 per cent low-velocity zone in the *S*-wave tomography (Keyser *et al.* 2000, 2002). See Fig. 11 for a direct comparison of the tomography images with the results of the RF migration of the data.

The addition of a high-velocity body of 40 km thickness and 200 km lateral extension (HVZ, *P*- and *S*-velocity increase of +2.4 per cent) in the forward modelling did not produced a visible effect in the section. Therefore, in the model used in Fig. 10 the *P*-wave anomaly was kept at +2.4 per cent in the HVZ, whereas the *S*-velocity anomaly in the HVZ was increased to +7 per cent, resulting in the sequence of red and blue at about 17.5 and 21 s, respectively (Fig. 10, right; see also Fig. 3a). This approach was guided by the results of the tomography for *P* and *S* waves (Fig. 11, left and centre) respectively, which show no *P*-wave anomaly at about 200 km depth but a remarkable velocity increase at about 200 km depth for the *S* waves (Keyser *et al.* 2000, 2002), see also discussion in the next section. If the lower bottom of the HVZ in Fig. 10 would not have been modelled as a sharp but rather a smooth transition like in Fig. 3(c), the blue signal at about 21 s would be missing, in agreement with the migrated data in Fig. 11 (right). The energy later than about 24 s in Fig. 10 (left), that is, below 300 km in Fig. 10 (right), is from the weak higher multiples from crust, LVZ and HVZ, respectively. Due to computational limitations in the forward

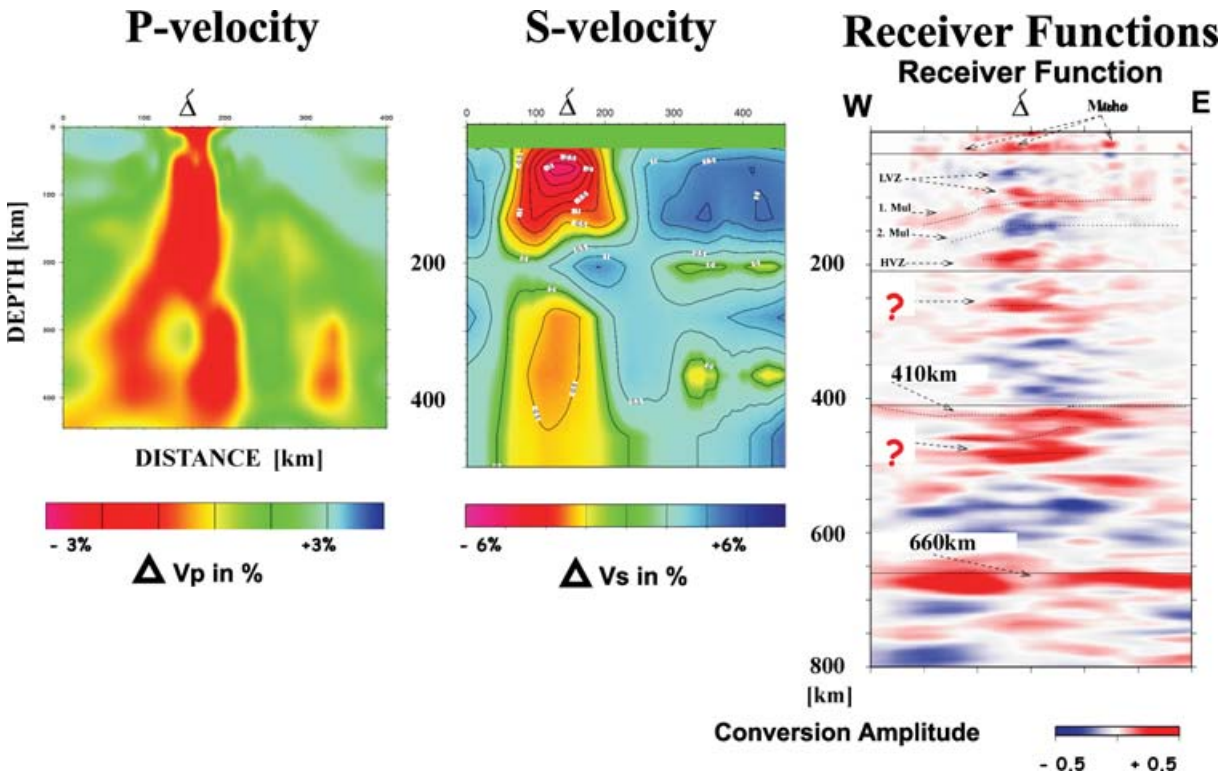

Figure 11. (Left) *P*-wave tomography results (Ritter *et al.* 2001). (Centre) *S*-wave tomography results (Keyser *et al.* 2000, 2002). The deviations in the *P*- and *S*-wave velocity are in percent and relative to IASP91, see also Fig. 3. (Right) Results of the migrated RF data (Fig. 5b) on an EW slice through the Eifel plume. The triangle at the top indicates the location of the Eifel volcanic fields.

modelling no absorption was included, however if absorption would have been included, these phases would be even more attenuated in the synthetics of Fig. 10.

Both, *P*- and *S*-velocity tomography models in Fig. 11, show an extension of reduced seismic velocities down to about 400 km depth, which is interpreted as the effect of the Eifel plume. Such a feature is most likely also the cause for the depression of 15 to 25 km of the 410 km discontinuity visible in the RF image (Fig. 11, right). Unfortunately, the Eifel network was not large enough to resolve structures deeper than about 400 km with tomography; therefore, the cause for the two additional large red anomalies in the RF image between 450 and 550 km depth (Fig. 11, right) cannot be studied independently.

In concluding this section it can be said, that the major features of the model in Fig. 10 down to 250 km depth, can be identified in the data. The migration, Fig. 11 (right) for the data and Fig. 10 (right) for the synthetics, properly images the sediment multiples and pulls in the diffractions of the LVZ. Furthermore, it was shown that it is possible to resolve seismic anomalies of a few percent contrast, a thickness of only 20 km and about 50 km lateral extension reliably in the uppermost mantle with the RF method for the frequency range used here (0.05 to 5 Hz).

6 DISCUSSION AND CONCLUSIONS

Analysis of the Eifel Plume data with the RF method confirms that a mantle plume feeds the volcanism of the Eifel. Fig. 12 shows a comparison of the 1-D IASP91-model with a best 1-D *S*-velocity model derived from seismic tomography and the RF study presented here.

The most convincing evidence for this model supporting the assumption that a plume exists under the Eifel are:

(1) Thinning of the crust under the Eifel by at least 2 km (slightly south of the volcanic fields, diameter *ca*. 100 km, Fig. 6).

(2) Detection of a low *S*-velocity zone between roughly 60–90 km depth under the West Eifel (diameter *ca*. 100 km, Fig. 7).

(3) A region of about 100 km thickness (100 to 200 km depth) with reduced *S* velocities (roughly under the Eifel, diameter about 100 km, Fig. 11; Keyser *et al.* 2000, 2002).

(4) Occurrence of an area with slightly elevated *S* velocities at about 200 km depth (under the West Eifel, diameter *ca*. 150 km, Fig. 8). This unusual feature could be due to *S*-wave anisotropy (see also Walker *et al.* 2005) which compensates for the elevated temperatures.

(5) From 250 to about 400 km depth, *P*- and *S*-wave tomography both show a plume-like structure (under the Eifel, diameter about 150 km, Fig. 11).

(6) The 410 km discontinuity is depressed by 15–25 km (south of the Eifel, diameter of about 200 km, Fig. 9, top) due to increased temperatures of +200°C to +300°C relative to the surrounding upper mantle (Bina & Helffrich 1994).

(7) Below the depressed 410 km discontinuity two additional positive *S* velocity jumps can be identified in the depth range between 450 and 500 km (roughly under the Eifel, diameter *ca*. 200 km; Fig. 5; Fig. 11, right). This could possibly be the (present day) source of the plume, but the lack of tomographic images and mineralogical/petrological data precludes further speculation at the moment.

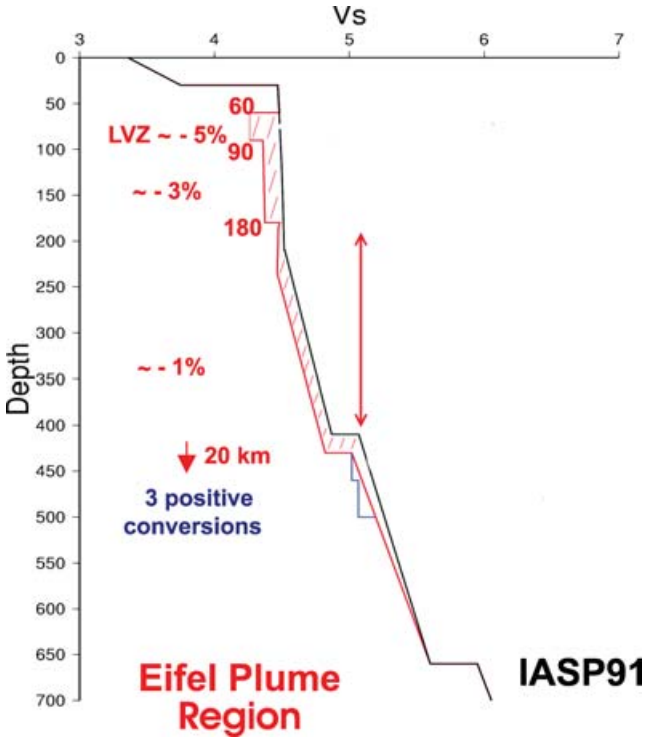

Figure 12. Comparison of the 1-D IASP91 *S*-velocity model (black) and the best 1-D *S*-velocity model under the Eifel (red) derived from seismic tomography and RF.

(8) The 660 km discontinuity seems unaffected by the plume (Fig. 9, bottom).

The most likely scenario for the Eifel plume is therefore a plume with a temperature increase of about +200 to +300 degrees. To decide, whether the Eifel Plume, now residing in the upper mantle, was originally connected to a larger plume in the lower mantle (see e.g. Goes *et al.* 1999, 2000) and was sheared from its deep root, for example, by the closing of the Tethis ocean, requires the inversion of larger tomographic data sets combining data from several field experiments like Eifel, Massif Central (Sobolev *et al.* 1997), TOR (Hossein Shomali *et al.* 2002; Wilde-Piorko *et al.* 2002; Alinaghi *et al.* 2003) and SVEKALAPKO (Bruneton *et al.* 2002; Alinaghi *et al.* 2003; Sandoval *et al.* 2004).

ACKNOWLEDGMENTS

We appreciate comments by J. Ritter, S. Sobolev and F. Schilling. We thank the Eifel Plume Team (U. Achauer, G. Bock, G. Bokelmann, M. Budweg, T. Camelbeeck, U. Christensen, F. Collin, N. d'Oreye, I. Eschghi, H. Gaensicke, K.-G. Hinzen, T. Kaspar, R. Pelzing, F. Scherbaum, Y.-F. Temme, K. Walker, M. Weber & U. Wüllner) and all people who assisted the seismological experiment for their help. Mobile recording instruments used for this study were supplied by the GeoForschungsZentrum (GFZ) Potsdam, the University of Potsdam, the Royal Observatory of Belgium and the Network of Autonomously Recording Seismographs (NARS) at Utrecht University. Further waveform data and instrument response functions were provided by Bundesanstalt für Geowissenschaften und Rohstoffe (BRG) Hannover, Germany (GRSN & GRF); GeoForschungsZentrum Potsdam, (GEOFON); Geological Survey Nordrhein Westfalen; Geological Survey Baden-Württemberg; ORFEUS Data Centre; Réseau National de Surveillance Sismique, France; Royal Observatory of Belgium (Belgian and Luxembourg National Networks); Seismological Division KMNI, Netherlands; Seismological Station Bensberg, University of Cologne. T. Ryberg provided his FD-modelling code. The numerical calculations of the synthetic seismograms were performed on the Cray T3E900/512 of the High-Performance-Computing Centre in Stuttgart. SeismicHandler (Stammler 1993) was used for the analysis of the seismological data and several figures were produced with GMT (Wessel & Smith 1998). The Eifel Plume Project and MB were supported by the Deutsche Forschungsgemeinschaft through grant Ch77/9-4 and by the GFZ Potsdam.

REFERENCES

Alinaghi, A., Bock, G., Kind, R., Hanka, W., Wylegalla, K., TOR. & SVEKALAPKO Groups, 2003. Receiver function analysis of the crust and upper mantle from the North German Basin to the Archean Baltic Shield. *Geophys. J. Int.,* **155,** 641–652.

Ammon, C.J., 1997. An *overview of Receiver Function Analysis*, http//www.eas.slu.edu/People/CJAmmon/HTML/RftnDocs / rftn01.html, Saint Louis University, St. Louis, Missouri.

Bina, C. & Helffrich, G., 1994. Phase transitions, Clapeyron slopes and transition zone seismic discontinuity topography, *J. geophys. Res.,* **99,** 15 858–15 860.

Birch, F., 1961. The velocity of compressional waves in rocks to 10 kilobars, Part 2, *J. geophys. Res.,* **66,** 2199–2224.

Bostock, M., 1999. Seismic waves converted from velocity gradient anomalies in the Earths upper mantle, *Geophys. J. Int.,* **138,** 747–756.

Brauer, A., Endres, C., Günter, C., Litt, T., Stebich, M. & Negendank, J.F.W., 1999. High resolution sediment and vegetation responses to Younger Dryas climate change in varved lake sediments from Meerfelder Maar, Germany, *Quaternary Science Reviews,* **18,** 321–329.

Brazier, R.A., Nyblade, A.A., Langston, C.A. & Owens, T.J., 2000. Pn wav e velocities beneath the Tanzanian Craton and adjacent rifted mobile belts, East Africa, *Geophys. Res. Lett.,* **27,** 2365–2368.

Bruneton, M., Farra, V., Pedersen, H.A. & the SVEKALAPKO Seismic Tomography Working Group, 2002. Non-linear surface wave phase velocity inversion based on ray theory, *Geophys. J. Int.,* **151,** 583–596.

Budweg, M., Weber, M., Bock, G., Ritter, J., Christsensen, U. & the Eifel-Plume Team, 1999. A 400 km long broad-band antennae in the Eifel region. *ORFEUS Electronic Newsletter,* **1**(3), http://orfeus.knmi.nl/newsletter/vol1no3/eifel.html.

Budweg, M., 2003. The upper mantle in the Eifel region studied with the receiver function method,Scientific Technical Report GFZ (in German), **STR03/04,** pg. 117. (http://www.gfz-potsdam.de/bib/pub/str0304/0304.pdf).

DEKORP Research Group, 1991. Results from the DEKORP 1 (BELCORP-DEKORP) deep seismic reflection studies in the western part of the Rhenish Massif, *Geophys. J. Int.,* **106,** 203–227.

Duncan, R.A., Petersen, N. & Hargraves, R.B., 1972. Mantle plumes, movement of the European plate, and polar wandering, *Nature,* **239,** 82–85.

Fee, D. & Dueker, K., 2004. Mantle transition zone topography and structure beneath the Yellowstone hotspot, *Geophys. Res. Lett.,* **31,** doi:10.1029/2004GL020636.

Goes, S., Spakman, W. & Bijwaard, H., 1999. A lower mantle source for Central European volcanism, *Science,* **286,** 1928–1931.

Goes, S., Govers, R. & Vacher, P., 2000. Shallow mantle temperatures under Europe from P and S wave tomography, *J. geophys. Res.,* **105,** 11 153–11 169.

Griesshaber, E., O'Nions, R.K. & Oxburgh, E.R., 1992. Helium and carbon isotope systematics in crustal fluids from the Eifel, the Rhine Graben and Black Forest, F.R.G., *Chemical Geology,* **99,** 213–235.

Grunewald, S., Kind, R. & Weber, M., 2001. The upper mantle under Central Europe indications for the Eifel plume, *Geophys. J. Int.,* **147,** 590–601.

Hirose, K., 2002. Phase transitions in pyrolitic mantle around 670-km depth: implications for up-welling of plumes from the lower mantle, *J. geophys. Res.,* **107,** doi:10.1029/2001JB000597.

Hock, S., Rothert, E., Ritter, J.R.R. & Korn, M., 2004. Mapping random lithospheric heterogeneities from the Baltic Shield to the Massif Central, France. *Geophys. J. Int.,* **157,** 251–264, doi:10.11117j.1365–264X.2004.02191.x.

Hossein Shomali, Z., Robertzs, R.G. & TOR Working Group, 2002. Nonlinear body wave teleseismic tomography along the TOR array. *Geophys. J. Int.,* **148,** 562–574.

Kelly, K., Ward, R., Treitel, S. & Alford, R., 1976. Synthetic seismograms: a finite difference approach, *Geophysics,* **41,** 2–27.

Kennett, B. & Engdahl, E., 1991. Travel times for global earthquake location and phase identification, *Geophys. J. Int.,* **105,** 429–465.

Keyser, M., Meyer, R. & Ritter, J.R.R., 2000. Teleseismic S-wave and Qp recordings at the Eifel plume project, in *Comptes-Rendus Journees Luxembourgeoises de Geodynamique*,Vol. 87, pp. 72–77, ed. Bonatz, M.

Keyser, M., Ritter, J.R.R. & Jordan, M., 2002. 3-D shear wave velocity structure of the Eifel plume, Germany, *Earth plantet. Sci. Lett.,* **203,** 58–82.

Langston, C.A., 1979. Structure under Mount Rainer, Washington, inferred from teleseismic body waves, *J. geophys. Res.,* **84,** 4749–4762.

Li, X., Kind, R., Priestley, K., Sobolev, S.V., Tilmann, F., Yuan, X. & Weber, M., 2000. Mapping the Hawaiian plume conduit with converted seismic waves, *Nature,* **405,** 938–941.

Li, X., Kind, R., Yuan, X., Sobolev, S.V., Hanka, W., Ramesh, D.S., Gu, Y. & Dziewonski, A.M., 2003. Seismic observation of narrow plumes in the oceanic upper mantle, *Geophys. Res. Lett.,* **30,** doi: 10.1029/2002GL015411.

Li, X., Kind, R., Yuan, X., Wölbern, I. & Hanka, W., 2004. Rejuvenation of the lithosphere by the Hawaiian plume, *Nature,* **427,** 827–829.

Lippolt, H.J., 1983. Distribution of volcanic activity in space and time, in *Plateau Uplift, The Rhenish Massif—A Case History*, pp. 112–120, eds Fuchs, K., von Gehlen, K., Mälzer, H., Murawski, H. & Semmel, A., Springer Verlag, Berlin.

Mechie, J., Prodehl, C. & Fuchs, K., 1983. The long-range seismic refraction experiment in the Rhenish Massif, in *Plateau Uplift, The Rhenish Massif—A Case History*, eds Fuchs, K., von Gehlen, K., Mälzer, H., Murawski, H. & Semmel, A., Springer Verlag, Berlin.

Meyer, W. & Stets, J., 1998. Junge Tektonik im Rheinischen Schiefergebirge und ihre Quantifizierung, *Z. dt. geol. Ges.,* **149,** 359–379.

Neugebauer, H.J., Woidt, W.-D. & Wallner, H., 1983. Uplift, volcanism and tectonics: Evidence for mantle diapirs at the Rhenish Massif, in *Plateau Uplift, The Rhenish Massif—A Case History*, pp. 381–403, eds Fuchs, K., von Gehlen, K., Mälzer, H., Murawski, H. & Semmel, A., Springer Verlag, Berlin.

Niu, F., Solomon, S.C., Silver, P.G., Suetsugu, D. & Inoue, H., 2002. Mantle transition-zone structure beneath the South Pacific Superswell and evidence for a mantle plume underlying the Society hotspot, *Earth planet. Sci. Lett.,* **198,** 371–380.

Passier, M.L. & Snieder, R.K., 1996. Correlation between shear wave upper mantle structure and tectonic surface expressions: Application to central and southern Germany, *J. geophys. Res.,* **101,** 25 293–25 304.

Raikes, S. & Bonjer, K.P., 1983. Large-scale mantle heterogeneity beneath the Rhenish Massif and its vicinity from teleseismic P-residuals measurements, in *The Rhenish Massif—A Case History*, pp. 315–331, eds Fuchs, K., von Gehlen, K., Mälzer, H., Murawski, H. & Semmel, A., Springer Verlag, Berlin.

Ritter, J.R.R., 2005. Small-scale mantle plumes: Imaging and geodynamic aspects, in Wenzel, F., ed., *Perspectives in modern seismology, Lecture Notes in Seismology*, **105,** Springer Verlag, Heidelberg, 69–91, doi:10.1007/b97731.

Ritter, J.R.R., 2006. The seismic signature of the Eifel plume, in Ritter, J.R.R. & Christensen U.R., eds, *Mantle Plumes – A Multidisciplinary Approach*, Springer Verlag, Heidelberg, in press.

Ritter, J.R.R., Achauer, U., Christensen, U.R. & the Eifel Plume Team, 2000. The teleseismic tomography experiment in the Eifel region, Central Europe: design and first results, *Seism. Res. Lett.,* **71,** 437–443.

Ritter, J.R.R., Jordan, M., Christensen, U.R. & Achauer, U., 2001. A mantle plume below the Eifel volcanic fields, Germany, *Earth. planet. Sci. Lett.,* **186,** 7–14.

Rothert, E. & Ritter, J.R.R., 2000. Scattering of teleseismic waves under the Eifel region, in *Comptes-Rendus Journees Luxembourgeoises de Geodynamique*,Vol. 87, pp. 78–81, ed. Bonatz, M.

Ryberg, T. & Weber, M., 2000. Receiver function arrays, a reflection seismic approach, *Geophys. J. Int.,* **141,** 1–11.

Ryberg, T., Tittgemeyer, M. & Wenzel, F., 2000. Finite difference modelling of elastic wave propagation in the Earth's uppermost mantle, in *High Performance Computing in Science and Engineering 1999*, pp. 3–12, eds Krause, E. & Jäger, W.), Transactions of the High Performance Computing Centre Stuttgart (HLRS), 1999, Springer, Berlin.

Ryberg, T., Tittgemeyer, M. & Wenzel, F., 2001. Modelling wave propagation phenomena in the Earth uppermost mantle, in *High Performance Computing in Science and Engineering 2000*, pp. 48–56, eds Krause, E. & Jäger, W., Springer.

Ryberg, T., Rümpker, G., Tittgemeyer, M. & Wenzel, F., 2002. Finite difference simulations of seismic wave fields in isotropic and anisotropic Earth models, in *High Performance Computing in Science and Engineering 2001*, pp. 35–47, eds Krause, E. & Jäger, W., Springer, Berlin.

Sandoval, S., Kissling, E., Ansorge, J. & SVEKALAPKO Seismic Tomography Working Group. 2004. High-resolution body wave tomography beneath the SVEKALAPKO array—II. Anomalous upper mantle structure beneath the central Baltic Shield, *Geophys. J. Int.,* **157,** 200–214. doi: 10.1111/j1365-246X.2004.02131.x

Schmincke, H.-U., Lorenz, V. & Seck, H.A., 1983. The Quaternary Eifel volcanic fields, in *Plateau Uplift, The Rhenish Massif—A Case History*, pp. 139–151, eds Fuchs, K., von Gehlen, K., Mälzer, H., Murawski, H. & Semmel, A., Springer Verlag, Berlin.

Shen, Y., Solomon, S.C., Bjarnason, I.Th. & Wolfe, C.J., 1998. Seismic evidence for a lower-mantle origin of the Iceland plume, *Nature,* **395,** 62–65.

Shen, Y., Wolfe, C.J. & Solomon, S.C., 2003. Seismological evidence for a mid-mantle discontinuity beneath Hawaii and Iceland, *Earth planet. Sc. Lett.,* **214,** 143–151.

Sobolev, S., Zeyen, H., Granet, M., Achauer, U., Bauer, C., Werling, F., Altherr, R. & Fuchs, K., 1997. Upper mantle temperatures and lithosphere-asthenosphere system beneath the French Massif Central constrained by seismic, gravity, petrologic and thermal observations, *Tectonophysics,* **275,** 143–164.

Spakman, W., van der Lee, S. & van der Hilst, R., 1993. Travel-time tomography of the European-Mediterranean mantle down to 1400 km, *Phys. Earth. planet. Inter.,* **79,** 3–74.

Stammler, K., 1993. SeismicHandler—programmable multi-channel data handler for interactive and automatic processing of seismological analyses, *Comp. Geosciences,* **19,** 135–140.

Vinnik, L.P., 1977. Detection of waves converted from P to SV in the mantle, *Phys. Earth planet. Inter.,* **15,** 39–45.

Walker, K.T., Bokelmann, G.H.R., Klemperer, S.L. & Bock, G., 2005. Shear wave splitting around hot spots: Evidence for a mantle up-welling related mantle flow, *Geophys. J. Int.,* **163,** 962–980.

Wessel, P. & Smith, W.H.F., 1998. New, improved version of Generic Mapping Tools released, *EOS, Trans. Am. geophys. Un.,* **79,** 579.

Wilde-Piorko, M., Grad, M. & TOR Working Group, 2002. Crustal structure variation from the Precambrian to Paleozoic platforms in Europe imaged by the inversion of teleseismic receiver functions-project TOR, *Geophys. J. Int.,* **150,** 261–270.

Yuan, X., Kind, R., Mechie, J. & Sandvol, E., 1997. Lithospheric and upper mantle structure of southern Tibet from seismological passive source experiments, *J. geophys. Res.,* **102,** 27 491–27 500.